12-2006

Acoustic Scattering from Mud Volcanoes and Carbonate Mounts

Charles W. Holland
Pennsylvania State University - Main Campus

Thomas C. Weber
University of New Hampshire, Durham, thomas.weber@unh.edu

Giuseppe Etiope
Istituto Nazionale di Geofisica e Vulcanologia, Rome, Italy

Acoustic scattering from mud volcanoes and carbonate mounds

Charles W. Holland[a)]
The Pennsylvania State University, Applied Research Laboratory, State College, Pennsylvania 16804-0030

Thomas C. Weber
University of New Hampshire, Center for Coastal and Ocean Mapping, Durham, New Hampshire 03824

Giuseppe Etiope
Istituto Nazionale di Geofisica e Vulcanologia, Rome, Italy 00143

(Received 5 April 2006; revised 8 August 2006; accepted 31 August 2006)

Submarine mud volcanoes occur in many parts of the world's oceans and form an aperture for gas and fluidized mud emission from within the earth's crust. Their characteristics are of considerable interest to the geology, geophysics, geochemistry, and underwater acoustics communities. For the latter, mud volcanoes are of interest in part because they pose a potential source of clutter for active sonar. Close-range (single-interaction) scattering measurements from a mud volcano in the Straits of Sicily show scattering 10–15 dB above the background. Three hypotheses were examined concerning the scattering mechanism: (1) gas entrained in sediment at/near mud volcano, (2) gas bubbles and/or particulates (emitted) in the water column, (3) the carbonate bio-construction covering the mud volcano edifice. The experimental evidence, including visual, acoustic, and nonacoustic sensors, rules out the second hypothesis (at least during the observation time) and suggests that, for this particular mud volcano the dominant mechanism is associated with carbonate chimneys on the mud volcano. In terms of scattering levels, target strengths of 4–14 dB were observed from 800 to 3600 Hz for a monostatic geometry with grazing angles of 3–5°. Similar target strengths were measured for vertically bistatic paths with incident and scattered grazing angles of 3–5° and 33–50°, respectively.
[DOI: 10.1121/1.2357707]

PACS number(s): 43.30.Gv, 43.30.Ma, 43.30.Vh [RAS] Pages: 3553–3565

I. INTRODUCTION

One of the important problems limiting active sonar performance in shallow water is the large number of false targets. Scattering that produces "target-like" echoes is defined here as clutter. Sonar clutter can arise from a variety of ocean features. High scattering has been observed from biologics (e.g., Ref. 1) and anthropogenic features such as wellheads and wrecks (e.g., Refs. 2 and 3). In shallow water, much of the observed clutter is believed to arise from features on and under the seabed. Seabed features (and the associated scattering mechanisms) that lead to clutter have not been well studied in the past; in particular the characteristic scattering and its dependencies upon incident and scattered vertical angle, azimuth and frequency are poorly understood.

One potential source of clutter from the seabed is mud volcanoes and carbonate mounds. Mud volcanoes form due to the rise of fluidized sediments and/or gas along a fault or on top of a seafloor-piercing shale diapir. They may occur in sedimentary areas with hydrocarbon generation at depth, originate from thick clay beds, usually erupt along fault lines, and often bubble gas (mostly methane), and sometimes oil. At least 300 mud volcanoes are known to exist on the ocean shelves,[4] mainly within the petroliferous basins. They are known to occur in a variety of geologic settings, including the abyssal parts of inland seas, active margins, continental slopes of passive margins, and continental shelves. A recent review article estimates the number of deep-water submarine mud volcanoes at 10^3–10^5.[5] Mud volcanoes studied along the Mediterranean Ridge at water depths ~2000 m are of order several 10^3 m in diameter and 10^2 m in height (e.g., Ref. 6). Deep-water mud volcanoes often are associated with gas hydrates.

Much less is known about shallow water mud volcanoes, and it is anticipated that continued advances in ocean exploration will bring new discoveries of mud volcanoes in areas presently not associated with mud volcanism. The recently discovered mud volcanoes in the Straits of Sicily[7] are much smaller (of order 10^1 to 10^2 in diameter and several meters in height) than their deep-water counterparts. They occur in water depths of 70–170 m (too shallow for gas hydrates) along the Scicli fault zone. Seismic reflection data (discussed in Ref. 7 and Sec. III B) show diapiric structures beneath cone-shaped structures, which are typical of mud volcanism. Though we do not have absolute proof that these features are mud volcanoes (a core sample would be required), we use the term mud volcanoes in the same sense as Ref. 8, given the apparent presence of carbonate mounds.

The objectives of this research were to identify the scattering mechanism associated with a single mud volcano

[a)]Author to whom correspondence should be addressed; electronic mail: holland-cw@psu.edu

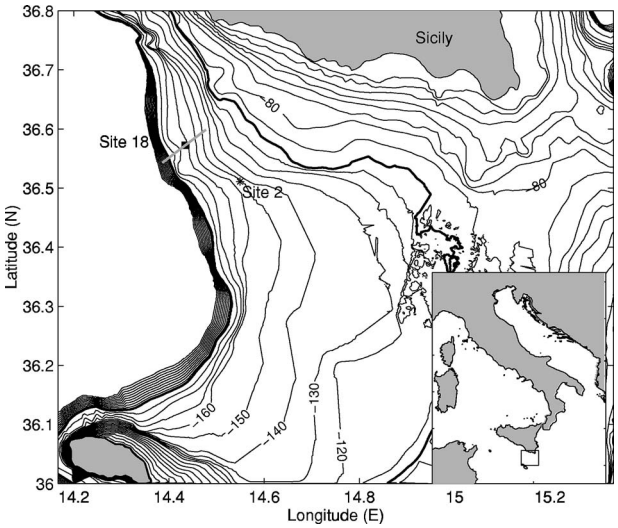

FIG. 1. Map of experiment area in the Straits of Sicily. The mud volcanoes of interest are located at Site 18. The black box at site 18 corresponds to the precise area of the multibeam measurements of Fig. 2. The gray line intersecting Site 18 is the sub-bottom profiling track (see Fig. 5). Seabed reflection measurements were conducted at Site 2.

(MV) and determine the frequency and angular dependence of the scattering. For the scattering mechanism, the three hypotheses that seem most probable are:

(1) gas bubbles (emitted) in the water column;
(2) gas entrained in sediment at/near mud volcano; and
(3) structure itself (carbonate pavements and/or chimneys)

The measurements were designed to determine which mechanism(s) play a significant role in the scattering and the commensurate clutter.

II. APPROACH

Through long-range reverberation, clutter features can be detected and localized. Long-range broadband (200–2000 Hz) reverberation measurements in the Malta Plateau (unpublished data) have shown significant clutter at the locations of some of the mud volcanoes (MVs). In the area of interest (see Site 18 box in Fig. 1) scattered returns from the MVs are 10–20 dB above the background reverberation and have been observed from distances up to 22 km. However, at long ranges, quantifying scattering characteristics of the feature, e.g., identifying the scattering mechanism, can be difficult or impossible. This is because uncertainties in the propagation paths, i.e., mechanisms dominating the propagation to and from the scatterer (both related to the oceanography and the seabed geoacoustics) are typically quite large.

An alternative approach is to probe the clutter features at close range using a direct path scattering technique. Direct path scattering observations offer two significant advantages: (a) the uncertainties associated with propagation (through a generally sparsely sampled ocean) are minimized, and (b) the measurement geometries are favorable to producing data from which hypotheses about the scattering mechanisms can be directly tested. Our experimental approach, adapted from a scattering technique designed for diffuse scattering, is discussed in more detail in Sec. IV A. Before discussing the scattering technique, we summarize (in Sec. III) what is known about the mud volcanoes from geophysical sensors and visual observations.

III. MUD VOLCANO CHARACTERISTICS

In order to identify potential scattering mechanisms, a variety of measurements were made on and around the MVs. These include bathymetry and seafloor backscatter data collected with a Reason 8101 240 kHz multibeam echo sounder, 300 kHz water column backscatter collected with an RDI acoustic Doppler current profiler (ADCP), and temperature, salinity, and dissolved oxygen above the suspected mud volcano using a Seabird CTD sensor. Additionally, an instrumented module (GAS-SCIPACK)[9] was deployed. These data were collected during the Boundary2004 Experiment within a few days of the low frequency acoustic scattering experiment (described later in Sec. IV). Seismic reflection data and sidescan data were collected during prior campaigns (2000 and 2002).

A. Multibeam bathymetry and backscatter

The experimental area, the Malta Plateau in the Straits of Sicily (Fig. 1), occupies the northern edge of the North African passive continental margin and is a submerged section of the Hyblean Plateau of mainland Sicily. While several

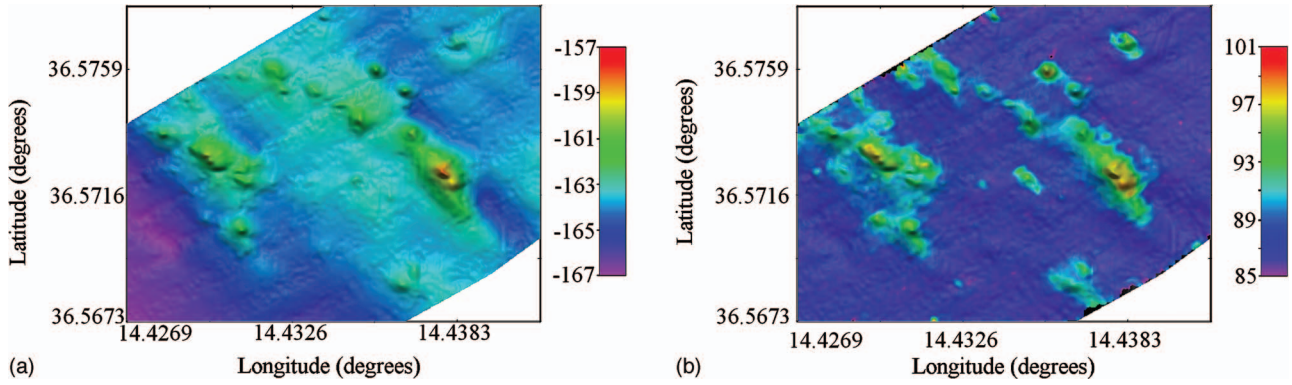

FIG. 2. (a) Multibeam bathymetry showing mud volcanoes at Site 18; the area is approximately 1350×1200 meters. Color corresponds to depth in meters. (b) A mosaic of values proportional to backscattering strength in dB (arbitrary units), corrected to 70°.

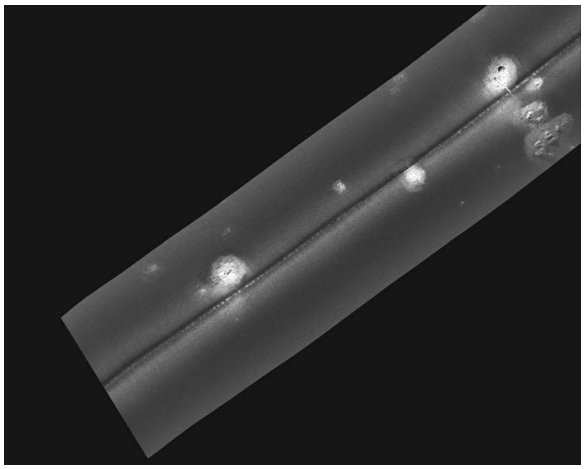

FIG. 3. Georeferenced 100 kHz sidescan image along the track (black line) in Fig. 7(b). The length of the track is approximately 1000 m and the cross-range dimension is 320 m.

clusters of mud volcanoes have been identified on the Malta Plateau, our interest here is focused on the MV cluster at Site 18 shown in Fig. 2.

The seafloor in Fig. 2 is gently sloped, from a depth of 164 m in the northeast corner of the survey to 167 m in the southwest corner. Several MVs are visible, rising to a maximum of approximately 5 m above the mean seafloor depth. The outer length scales observed in these features are quite variable, ranging from 40 to 400 m. Also visible in the data are nearly linear depressions adjacent to some of the larger MVs that may be associated with faults and/or regions of fluid escape. The multibeam sounding resolution varied across the swath from approximately 4 to 10 m in the across-track direction, and 2.5 m in the along-track direction. In postprocessing, the data have been low pass filtered, so that the resolution of in Fig. 2 is approximately 10 m.

An acoustic backscatter value associated with each multibeam bottom detection (one value for each beam on every ping) was also recorded in the raw multibeam data record. In order to compare different areas on the seafloor, these data were first corrected for any range and angle dependencies not associated with seafloor characteristics (similar to Ref. 10). Our main interest here is only in distinguishing between different types of seafloor, and so only relative backscatter values are required.

The strong angular dependence in the backscatter makes it difficult to identify different seafloor types in the data, and so the backscatter data are converted into a mosaic of values representing the backscatter that would be expected at a fixed grazing angle (70°). For each backscatter value, this is done by subtracting a predicted difference (in dB) for the backscatter at its true grazing angle from the predicted backscatter at 70°. Predicted backscatter values are derived from an empirical second degree polynomial fit that describes the angular dependence of all of the backscatter data within 40 m of the backscatter value in question. Although this method can introduce artifacts into the resulting mosaic, these artifacts should be on scales that are less than approximately 40 m, and the larger scale seafloor structure should remain largely unchanged.

The result of this process is shown in Fig. 2(b). Note that for each of the MVs (bathymetric highs) the corresponding scattering is relatively high. In general, for regions between

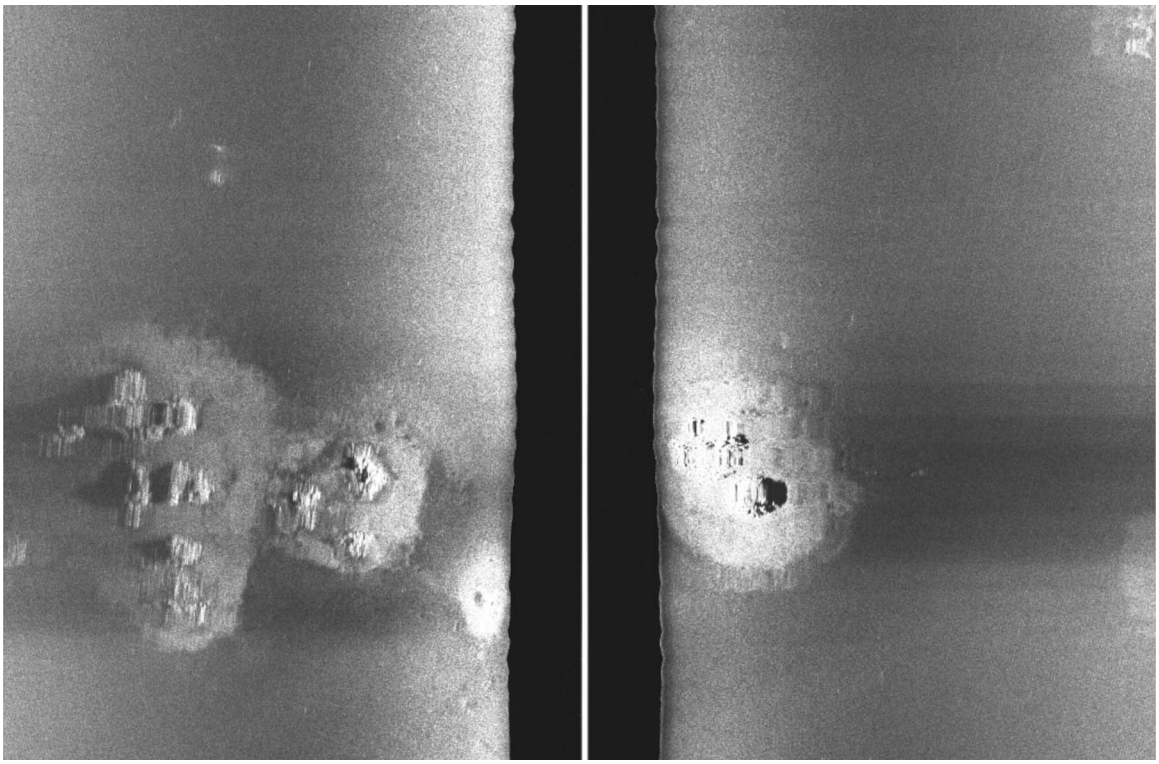

FIG. 4. A 100 kHz raw sidescan image (from Ref. 7) of the northernmost MV of Fig. 3 and the largest mound of Fig. 2. The scale is 320 m in cross range with approximately square pixel size; white indicates high scattering. The data indicate protrusions or carbonate chimneys on the MV roughly 10 m in lateral dimensions and 2–4 m in height. The altitude of the sonar was 19 m above the seabed.

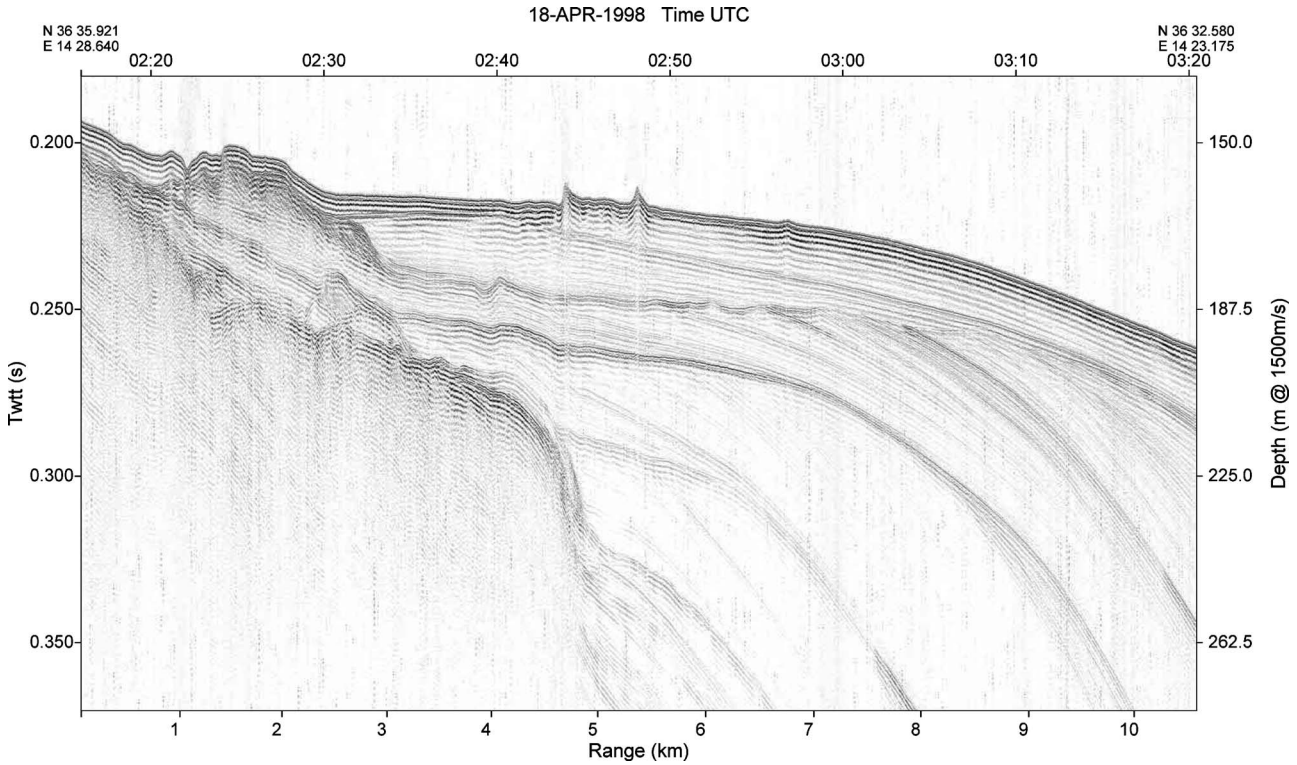

FIG. 5. Seismic reflection data showing the mud volcanoes (between 4 and 6 km). Vertical exaggeration is 350:1. The track location is shown as a gray line in Fig. 1.

the bathymetric highs, the scattering strength is lower. However, there are several discrete high scattering patches that do not correspond with an apparent bathymetric high (which might be because there are small mounds below the multibeam resolution). The backscattering data show three distinct regions: the background (~87 dB, arbitrary units that are proportional to acoustic backscatter), intermediate regions that are 2–4 dB above the background, and high backscatter regions which are 6–10 dB above the background. These three regions will be discussed again in the context of the visual observations (Sec. III C).

B. Seismic reflection and sidescan sonar

Sidescan data (Fig. 3) were collected using an Edgetech DF-100 along a 6 km line that cut through the central part of the multibeam survey box [see thick gray line in Fig. 7(b)]. The sidescan data clearly show three groups of features with high scattering; the easternmost and westernmost features can be clearly seen in the multibeam bathymetry and backscatter data (Fig. 2). The high scattering from near the center of the image does not have a clear counterpart in the bathymetry [Fig. 2(a)] but does in the multibeam backscatter data [Fig. 2(b)]. Raw sidescan data at the largest mound (Fig. 4) show protrusions on the mound roughly 10 m in lateral dimension and up to 4 m in height (calculated from the shadow length). From the shadow characteristics (also see Fig. 4 of Ref. 7) these protrusions appear to be constructed of cemented or consolidated sediment. These protrusions are believed to be carbonate chimneys. Note that the carbonate chimneys are not resolved in the multibeam data (Fig. 2).

Sub-bottom seismic reflection data were collected with an EG&G Uniboomer (Fig. 5). The western most and easternmost MVs are clearly seen at around 5 and 5.5 km, respectively. Note the indication of an acoustic shadow underneath the MVs which might be caused by the high impedance associated with the mounds, or possibly gas. Deeper layers show no clear indications of gas.

C. Geochemical and visual

Geochemical and visual oceanographic observations were performed using the GAS-SCIPACK module, an instrumented module for casts and towed surveys close to the seabed.[9] The module was equipped with two solid-state methane sensors (K-METS, Capsum, Germany), CTD and transmissometer (Idronaut 316), 12 Niskin 2.5 l bottles (General Oceanics 1015), echo sounder (Tritech PA500), color camera (Deep Sea Power & Light MULTI-SEACAM 2050 color), Light DL 1040 (120 V/250 W), attitude sensors (heading, pitch, roll) and internal status sensors (internal T, voltage, current, water detector). Sensor data and images were displayed in real time in an onboard console composed by a PC, TV, and video recorder. GAS-SCIPACK depth and direction were controlled following communications among console operators, winch driver, and navigating officer. Tow depths were typically a few meters above the seafloor. Though measurements were conducted at eight different sites on the Malta Plateau, we report here mainly on the Site 18 results.

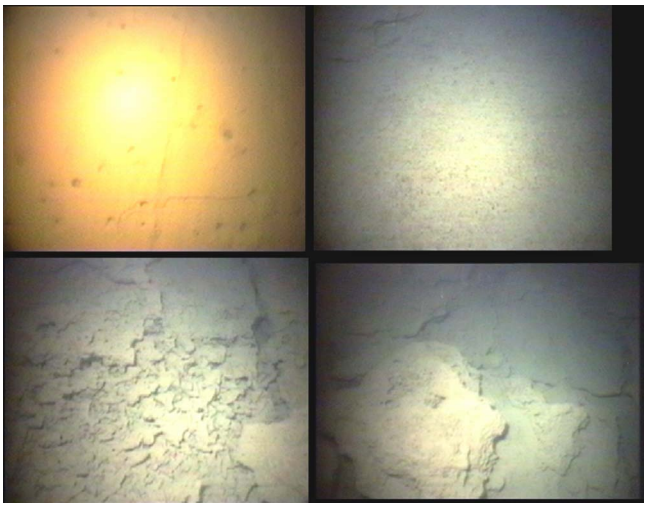

FIG. 6. Seafloor images (left to right) from the study area exhibiting (a) a soft fine-grained sediment; (b) coarse grained sediment surrounding the MVs; (c)-(d) carbonate heterogeneous crust and blocks on the MVs, ranging from centimeter to meter scale. The field of view is approximately 3 $\times$2.5 m.

1. Visual inspection

Bubbles were not visually detected at any of the eight sites. Two of the sites showed enriched benthic and pelagic biomass (Gorgonia, worms, fishes) and calcareous algae fixed on apparently cemented sediments. Only Site 18 (where the scattering measurements were conducted, see Fig. 1) was characterized by large and heterogeneous blocks without significant biomass. Such features are known to occur over mud volcanoes and in methane seepage areas. The images do not show classic mud volcanic edifices or mud flows, but these can be covered by the bio-constructions. The seismic profiles (see Fig. 5 and Ref. 7) suggest more clearly the occurrence of outcropping and buried mud volcanic (diapiric) structures.

The underwater video observations from Site 18 indicate seabed variability that is characterized by three distinct classes. The seafloor image in Fig. 6(a) shows a very soft, fine-grained sediment with evidence of bioturbation, which is characteristic of large areas of the seafloor a few tens of meters away from the MVs. This soft seafloor is in stark contrast to the seafloor image shown in Figs. 6(c) and 6(d) over the MVs. A third seafloor type—Fig. 6(b), found on the perimeter of the MVs, appears to be coarse-grained material (presumably weathered/eroded material from the carbonate mounds) and shows no evidence of bioturbation. These three bottom types—fine-grained, coarse-grained, and carbonate blocks and fragments—correspond reasonably well to the three different 240 kHz backscatter regions: background, intermediate, and high backscatter, respectively (see Sec. III A).

2. Methane analysis

A total of 18 seawater samples were collected at eight sites. Seawater samples were collected in 200 ml glass bottles, sealed with silicon septa and aluminium caps. Methane analyses were performed on board by head-space extraction (double syringe technique[11,12]), in thermostatic conditions, and GC-FID (gas chromatography-flame ionization detector); Autofim II, Telegan, UK; detection limit 0.1 ppm, accuracy 4%–5%. The reproducibility of replicate head-space samples was within ±15%, as determined from ten water samples in atmospheric equilibrium. Calibration was performed using atmospheric samples and Scotty II standards.

Concentrations of methane above 2–4 *n*Mol/l (equilibrium value with the atmosphere at the site-specific salinity temperature) are considered anomalous. Methane anomalies (tens of *n*Mol/l) were detected in all seawater samples collected close to the seafloor sediments. The highest concentrations (>200 *n*Mol/l) were found at two locations (36.4275° N 14.6434° E and 36.5708° N 14.4313° E) exhibiting similar bathymetric features as in Fig. 2. The latter location corresponds to Site 18—close to the location of the acoustic scattering measurements. At Site 18 a concentration of 300 *n*Mol/l was measured.

The solid-state methane sensors provided three pieces of useful information. First, they confirmed background levels of tens of *n*Mol/l across the area. At locations where the GC-FID showed high levels of methane, the solid-state sensors generally did not detect an increase. This is attributed to the relatively slow response time of the sensors (2–3 min). Second, given the response time and the drift speed of the vessel (less than about 1 knot), the indication is that the high levels of methane must exist over lateral dimension much smaller than ~50 m (at several meters above the seafloor). Finally, the sensors are quite sensitive to the presence of bubbles; however, no bubbles were detected during any of the tows.

D. ADCP and CTD drift results

Acoustic backscatter data from the hull-mounted ADCP on *R/V Alliance* were collected during one night where the *R/V Alliance* rotated between several MVs at Site 18, performing station keeping maneuvers for 20–45 min at each position. An example of the data collected corresponding to one of the four ADCP beams is shown in Fig. 7(a), with the ship's position during this time shown in Fig. 7(b). There are two distinct types of features in this data: (1) a group of scatterers spread over the entire bathymetric feature in a thin layer at a nearly constant depth of ~95 m, and (2) one or more plumes that are relatively large in their vertical extent (between 100 and 150 m). The acoustic backscatter in the horizontal layer is much lower than the backscatter from the vertical plumes, indicating that these are clouds of scatterers with either different number densities, different types, or both. Further, note that the plumes present over the mound located at 36.5725 N, 14.438 E between 01:10 and 01:55 local time appear to be gone $5\frac{1}{2}$ h later, although it is possible that the ADCP beam simply did not intersect the plume at that later time. The plumes found at 36.573 N, 14.430 E are present during both times that the ship was at that station. Measurements with a SeaBird CTD system (with an SBE 43 Oxygen sensor) taken between 22:08 and 22:51 local time several nights later show a very slight increase in dissolved

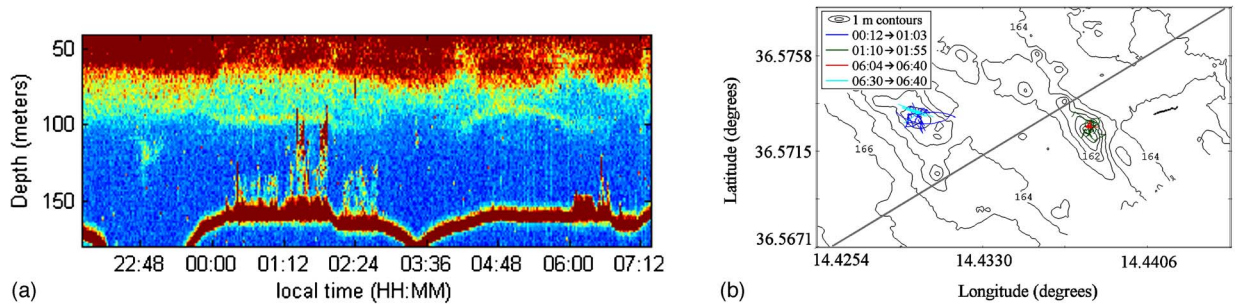

FIG. 7. (a) Acoustic backscatter from a single beam of the ship-mounted ADCP. (b) Tracklines including ADCP drift less than 0.5 m/s (colored lines); drift for low frequency scattering measurement (black short curved track ENE corner of plot); sidescan and seismic reflection track (diagonal gray line).

oxygen over the largest MV as compared to the surrounding regions (slightly less than a 1% difference).

These data indicate that a chemotrophic food chain may be present, where the base of the food chain uses methane rather than photosynthesis as its energy source (similar to that described for pockmarks found in the North Sea, (Ref. 13, see page 56]). Such a food chain may also support plankton and possibly nekton, which seems the most likely cause of the "plumes" in the ADCP backscatter data. Hovland and Judd[13] also suggest that fluid seepages can suspend nutrients that would otherwise be trapped in sediments, acting as an alternate mechanism at the base of the food chain. Although no evidence of seepage was found during the CTD drift, it is difficult to rule this out because of the possibility that the seepage is episodic. Another hypothesis that could explain the backscatter in the water column is that bubbles are being released from the sites where mounds are present. If this were happening, however, the O_2 anomaly would be expected to have the opposite sign, since dissolved oxygen would be diffusing into the methane bubbles as they rose through the water column, e.g., Ref. 4 (although the ADCP and the CTD measurements were not taken simultaneously).

E. Summary observations

Mud volcanoes of sizes $O(10^{1-2})$ m in lateral dimension and several meters in height were observed on the outer shelf of the western Malta Plateau. There was no biomass observed on these MVs (in contrast to significant biomass observed on MVs roughly 25 km to the southeast). This may be because this is an active or recently active site, so that there may be insufficient time for biomass to have developed. The presence of high aqueous concentrations of methane near the MVs is certain, although there was no clear indication of gas in bubbles either in the sediment or in the water column. Between the sidescan and multibeam data our picture is of protrusions or carbonate chimneys roughly 10 m in lateral dimension and several meters high that are sometimes isolated but typically clustered on larger mounds.

Given the observations, it appears that the most likely mechanism for low frequency scattering is scattering from the carbonate mound itself and/or the carbonate chimneys on top of the mounds. While no measurements have been made on the material, it is apparently consolidated and so would have a relatively large impedance contrast relative to the water column which means not only that the scattering could be potentially large, but that scattering from within the MV (e.g., from gas bubbles entrained in the sediment) might be relatively hard to detect. While the observations suggest the lack of free gas bubbles, perhaps none of the hypotheses can be completely ruled out due to the potentially episodic nature of gas release.

IV. LOW FREQUENCY SCATTERING MEASUREMENTS AND MODELING

The objective of the low-frequency (800–3600 Hz) scattering experiment was to measure the scattering associated with a single mud volcano at close range. The MV selected for the scattering measurements, the largest mound in the cluster (at 36.5716° N 14.4383° E in Fig. 2), is roughly elliptical with dimension 150 m × 50 m and oriented at 145° (re North).

During the measurement period (1559–1609 UTC 21 May, 2004) the winds were light, less than a few m/s, with a sea state 1 and the vessel drifted along the track shown in Fig. 7(b), about 75° relative to the axis of the MV.

A. Experiment design

The main challenge of the short-range scattering experiment is to avoid or control multipaths. One multipath problem is potential contamination by sub-bottom reflections. It is well known that scattering may arise from not only the interface but also from sub-bottom inhomogeneities or horizons. However, sub-bottom reflections at normal incidence contaminate the scattering measurement, since the normal incidence reflections (even from sub-bottom horizons) are often at higher amplitude than scattering at lower angles.

A second multipath problem is contamination from hybrid paths. Hybrid paths are paths that belong to a different family of scattering events that arrive at the same time as the scattering path that is being measured. Figures 8 and 9 show the various paths and their relationship in time and angle. For example, in this geometry, beyond about 0.4 s, the monostatic (path *a*) and vertically bistatic paths (*b*, *c*, and *d*) cannot be separated in time or angle. By vertically bistatic we mean that the incident and scattered angles are different in the vertical plane. A receive and/or source array with vertical aperture can be used to control both types of multipaths, i.e., by reducing the contribution of the normal incidence reflections and also providing some discrimination against the various scattering paths.

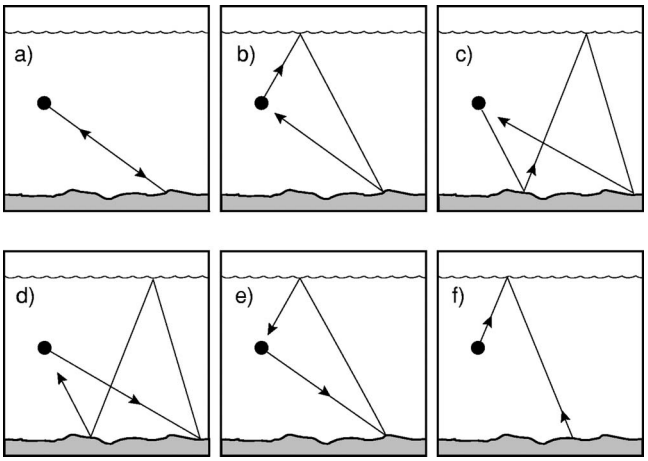

FIG. 8. Seabed scattering multipaths (from Ref. 15). Only those paths that have less than two surface interactions are depicted.

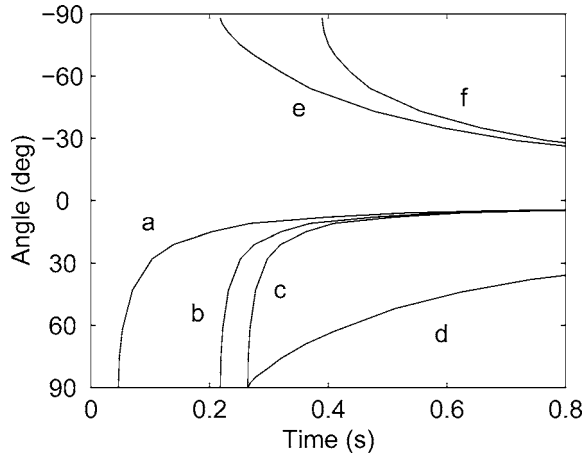

FIG. 9. Vertical arrival angles vs time for various bottom scattering paths. Time is referenced to source initiation. The geometry corresponds with the geometry of the experiment. Angles are measured with −90° towards the sea surface. Path (a) is the monostatic backscattering path. See Fig. 8 for other path descriptions.

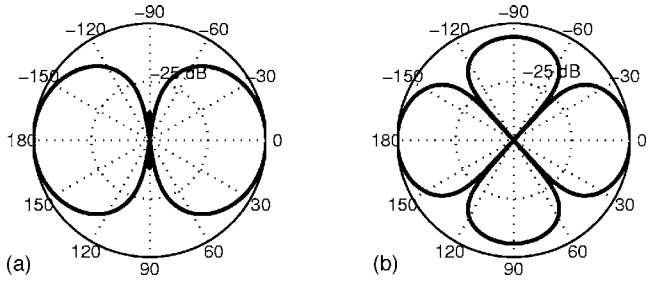

FIG. 11. Theoretical source beam patterns for: (a) 3600 and 1800 Hz and (b) 2400 Hz. The inter-element spacings for the three frequencies were 20.8, 41.7, and 41.7 cm, respectively. The beam pattern at 800 Hz is omnidirectional (a single Mod 40 transducer was employed). For analysis in this paper, only transmitted paths near 0° are employed, where the theoretical curves are quite accurate.

Figure 10 depicts the system employed in this study. The vertical aperture of the receive array helps minimize effects of multipath. Short pulses (typically 15 ms) from transducers near the bottom of the array provided a repeatable and stable source. The equipment is deployed from the forecastle and the ship was left to drift. The weight of the Mod-40s (90 kg in water) provides enough ballast to keep the array straight when the current shear is small. A small fin (not shown) on the Mod40 frame stabilizes the array against rotational forces.

The source array was constructed with pairs at $\lambda/2$ spacing in the vertical so that transmitting in phase would yield a null in the vertical plane. The mid-frequency source array was constructed of 3 ITC-4001 transducers spaced at 20.8 and 41.7 cm, to yield $\lambda/2$ spacing at 3600, 1800, and 1200 Hz. The top of this array was placed 1 m below the bottom phone of the receive array. The low frequency array consisted of 2 Mod 40 flextensional transducers spaced at 1.27 m (or $\lambda/2$ spacing at ~600 Hz). Theoretical beam patterns are shown in Fig. 11. Beam pattern measurements (see Ref. 15) showed some deviations from the theoretical re-

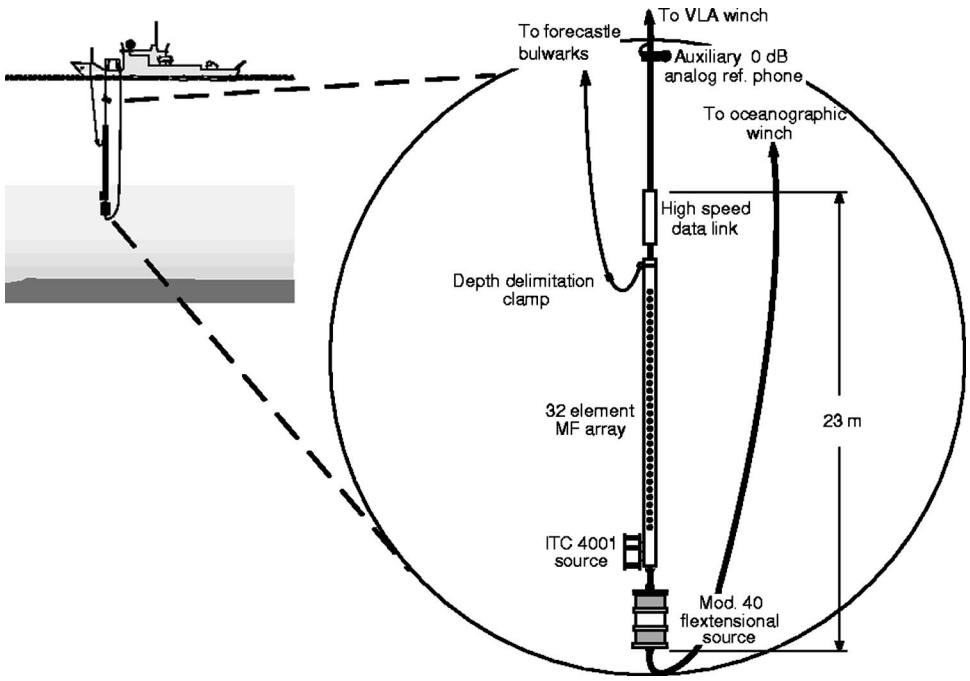

FIG. 10. Experiment geometry used for measuring bottom scattering (from Ref. 15). Details of the source and receive arrays are found in the text.

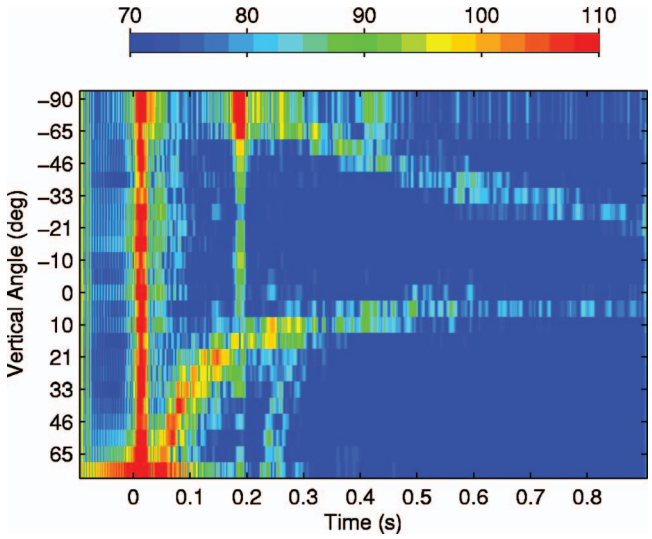

FIG. 12. Scattering (in dB) from a "uniform" seabed as seen by the vertical array from a single ping at 3600 Hz. The various paths evolution in time and angle correspond to those shown in Fig. 9. The arrival at 0.18 s, observed on nearly all beams, is the surface reflected path.

sponse, but the differences are not significant for this study, since the focus is on low grazing angle scattering that would be important for long-range clutter. Ping types included both CW and LFM pulses of 15 ms pulse length. Repetition rates of 6 pings/min were used, and the acquisition system was triggered 1 s before transmit to acquire ambient noise for each ping. Fifteen pings were collected for each frequency.

The receive array consisted of 32 Benthos AQ-4 hydrophones with a 0.18 m spacing hardwired directly to the NATO Research Vessel (NRV) *Alliance*. The data were sampled at 12 kHz and low pass filtered at 3.8 kHz with a seven-pole six-zero elliptic (70 dB per octave roll off) antialias filter. The RC high pass filter (6 dB per octave roll off) was set at 500 Hz. A high speed digital link within the array provided programmable signal conditioning, digitization, and serialization of the signals. Following signal conditioning, data were beamformed (Hanning shading) using a plane wave time domain beamformer.[16] Beams were spaced to yield 3 dB down crossing points at the design frequency of the array. The data are filtered in 200 Hz bands with a sixth order low pass digital elliptic filter with 0.5 dB of ripple in the passband and a stopband 50 dB down. Receive array depth and the total water depth are determined using the arrival times of the surface and bottom reflected paths.

Experimental results from a control area (i.e., flat seabed) are shown in Fig. 12. The water depth and source depth are 128 and 91 m, respectively. Zero time in the figure corresponds to the direct blast, which overloads the array and is seen on all beams. The surface reflection is visible at 0.18 s. Clear arrival paths can be understood in terms of the various monostatic and bistatic scattering paths of Figs. 8 and 9. This experimental method has been used in the past (e.g., Refs. 15 and 17) to obtain diffuse scattering strength, i.e., scattering strength versus angle for seabeds that are homogenous (in a gross sense) over scales of hundreds of meters. In the following, we adapt the method to be able to measure scattering from discrete scatterers.

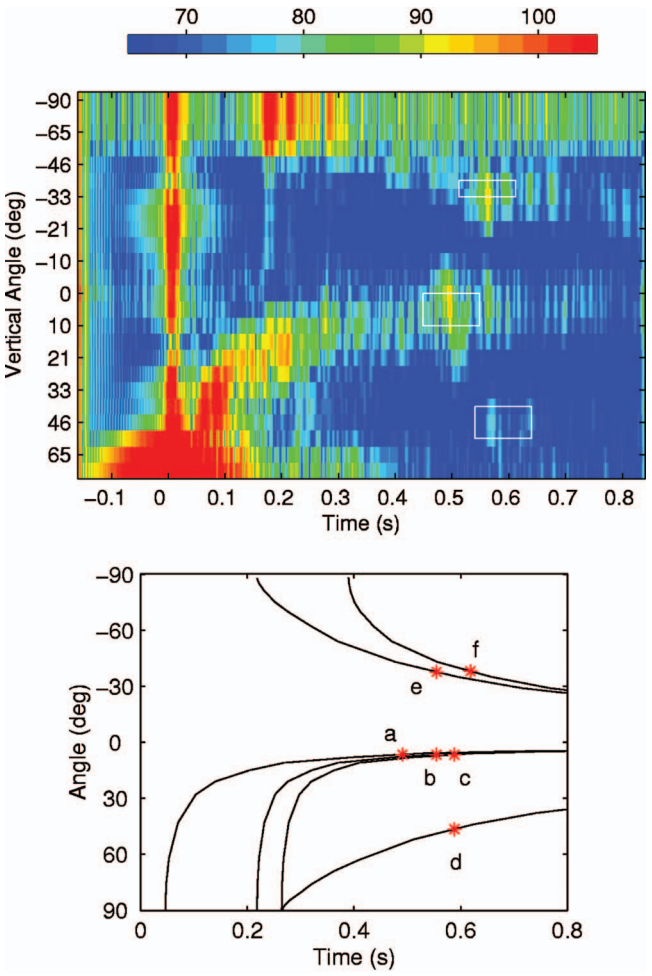

FIG. 13. Scattering at 1800 Hz (in dB) from a single ping along track 5. The scattered arrivals from the MV are clearly observed along several paths and are highlighted by the white boxes. Note returns from direct-direct (path a), direct-surface reflected (path e) and surface bottom (path d). The surface-direct (path b) can also be faintly seen at the same time as the direct-surface (path e) and on the same beam as the direct-direct (path a). The path geometries are shown in Fig. 8. The key points of the figure are that scattering from the MV is ~10–15 dB above the scattering from the surrounding seabed, that the scattering occurs at grazing angles slightly lower (closer to the horizontal) than from the background sediment, and finally that there is no significant scattering in the water column.

B. Scattering from the MVs

An example of the measured beam time series near the MV is provided in Fig. 13(a). A discrete scatterer would be expected to be visible in the beam time series along one or more of the various paths [see Fig. 13(b)]. The scattering from the MV can be seen on the monostatic path (path *a*) at about 0.48 s and is ~10–15 dB above the diffuse scattering from the surrounding seabed. The angle associated with this path and range is +5° (i.e., 5° down). The bistatic MV-surface reflected path (path *e*) is seen at −40° at 0.55 s. The reciprocal path (surface-MV or path *b*) occurs at the same time but at +5°. Note that its level is reduced relative to path *e* because of the source beampattern. The MV-surface-bottom path (path *d*) occurs at 0.57 s and a scattered angle of about 45°.

One of the important aspects of the analysis pertains to identification of the scattering mechanism. Each of the hy-

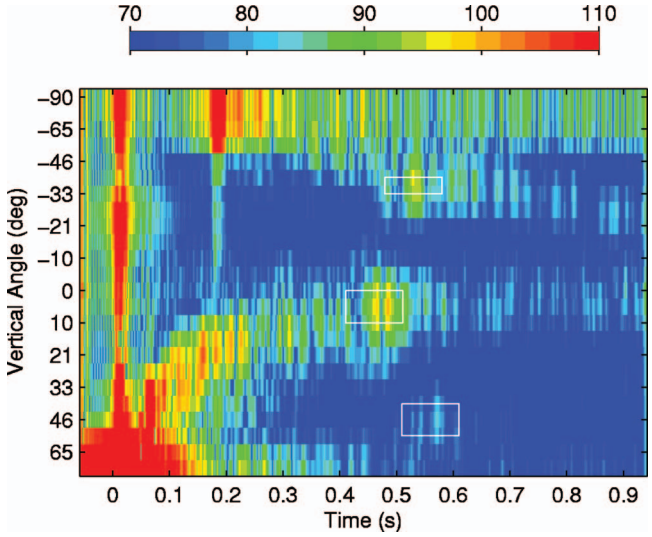

FIG. 14. Multiple scattered returns from the MV could be observed occasionally (see the two closely spaced returns on the direct-direct path).

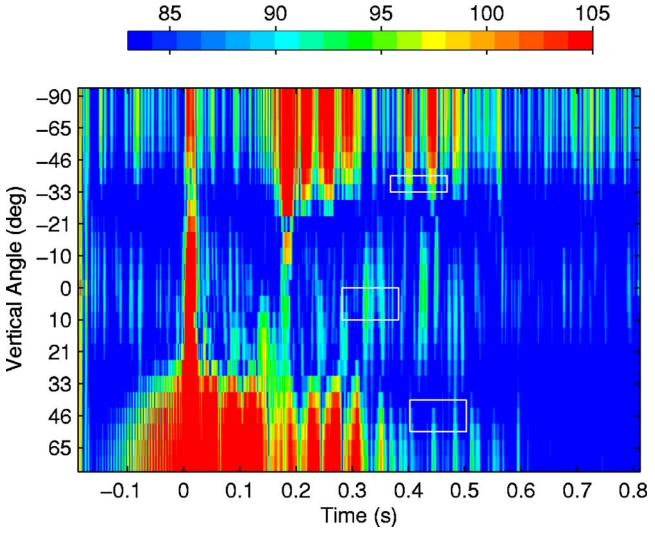

FIG. 15. (Color online) Beam time series at 800 Hz showing the direct-direct, surface-direct and direct-surface-bottom scattering paths. The direct-surface path is obscured because of the wide beams and the surface scattered paths. The direct path (white box at about 5°) is visible along with the surface-direct path on the same beam 0.1 s later.

potheses can be examined in light of the beam-time series data [Fig. 13(a)]. Hypothesis (1) was that the dominant scattering mechanism was from bubbles and particulates emitted from the MV. If this hypothesis was correct, then we would expect to see high scattering in the water column (i.e., in the beams corresponding to 0° to −48° (the angle associated with surface scattering at that range). However, there is no evidence in the data of scattering within the water column (scattering levels in the water column are ~40 dB lower than the scattering from the seabed). The data indicate that hypothesis 1 is not correct during the time period of the observations.

Hypothesis 2 stated that the dominant scattering mechanism was from gas trapped under, around or within the MV. Inspection of Fig. 13 shows that the strongest arrival is actually a few degrees higher than the scattering from the surrounding seabed at the same instant in time. It is easiest to see this on the monostatic path, path *a*. This means that the scattering is coming from above the seabed (though the vertical resolution is insufficient to quantify how high). In Fig. 14, beam time series are shown for a different ping. In this ping several scattering highlights on given path from the MV are apparent (seems to occur in less than 50% of the pings). These events occur 18 ms apart (27 m in round trip travel) and it seems most likely that they come from two distinct features on the MV. At 800 Hz (Fig. 15), the receive beams are so wide in the vertical, that it becomes nearly impossible to distinguish paths *d* and *e* from surface scattering and bottom scattering events. Since the source beam pattern is omni directional, generally both paths *a* and *b* are visible.

Hypothesis 3 was that the dominant scattering mechanism was from the structure itself. The evidence from the beam-times series data indicates that this is the most likely mechanism. Futhermore, it seems most likely that the scattering arises from the carbonate chimneys which rise from the top of the MV. However, bubbles in the MV itself (but higher than the water depths surrounding the MV) cannot be completely ruled out.

C. Target strength estimation

The scattered intensity I from the MV can be written:

$$I = I_o \delta_i \delta_s s_t, \tag{1}$$

where I_o is the source intensity, $10\log_{10}(s_t)$ is the target strength and δ is a transmission factor from the source to the scattering patch (subscript i) and the reverse path (subscript s); $-10\log_{10}(\delta)$ is the one-way transmission loss). The scattered intensity is measured by taking the peak level within a small time window around the expected arrival time. The source intensity was monitored by a hydrophone above the source, but since the hydrophone is in the null of the source beam pattern, a more robust estimate was made using the recorded power amplifier drive voltage and the calibrated transducer response curves.

The transmission factors are estimated by assuming spherical spreading. This is reasonable since the sound speed profile is nearly isovelocity near the seabed (see Fig. 16) and the surface reflected paths are at steep angles (>30°). For the angles probed, the difference between the two-way transmission loss using the isovelocity assumption and that using the measured profile is less than 1 dB and the difference in angles between source and receiver above 3° is less than 0.3°. Assuming incoherent summation of paths:

$$\delta_i \delta_s = \frac{N_i}{r_i^2} \frac{N_s}{r_s^2} \prod_{m=1}^{M} R_m, \tag{2}$$

where r is the distance along the path (incident i or scattered s), N is the number of arrivals that contribute within the pulse length, and R is the intensity reflection coefficient from M boundary interactions. Assuming that the scattering event takes place on the MV (i.e., elevated somewhat relative to the surrounding seabed) both the direct and the bottom reflected paths contribute to the observed scattering (see Fig. 16). The direct and bottom reflected paths arrive at the scat-

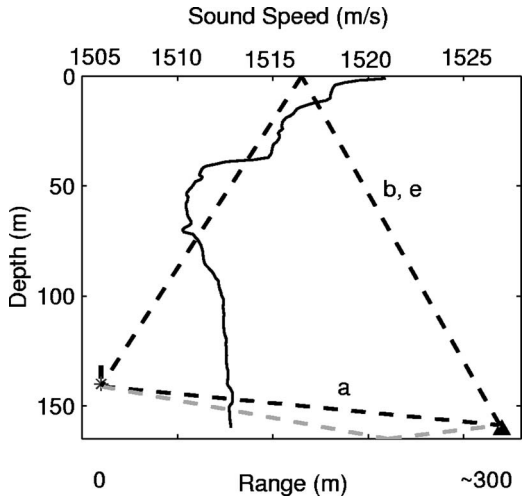

FIG. 16. Sound speed profile and geometry of the experiment showing the source (*), receiver (|) MV (▲) and ray paths (---). Vertical exaggeration is 2:1. The ray paths are identified by the labels of Fig. 8. For clarity, path d is not shown, but is similar to paths b,e with a bottom reflection following the surface reflection.

tering patch within less than a millisecond (i.e., much smaller than a pulse length) so $N_i=2$. For the monostatic[18] path (path a) since the paths are reciprocal $N_s=2$. However, for the bistatic paths (paths b, d, and e) the receiver is high enough above the seabed that only one path contributes, $N_s=1$.

The reflection coefficients of the seabed R_b and sea surface R_s are estimated in the following way. For the monostatic path, path a, R_b is required at 5–6° grazing (depending on the range between source and MV). These angles are below the critical angle (approximately 12°) so $R_b \sim 1$. The exact reflection coefficient below critical angle depends upon the attenuation which is not known to very high accuracy, nevertheless the error in target strength induced by the approximation $R_b=1$ is expected to be very small. For path d (direct-surface-bottom path), an estimate of R_b (39–51°) is required for 1800–3600 Hz and spherical wave reflection coefficient measurements at a similar water depth (Site 2, for see location in Fig. 1) are used as a proxy. At large kd (where k is the wave number and d is the distance from source to bottom to receiver) the spherical and plane wave coefficients are very similar. For the reflection coefficient measurements $d>180$ and $k>7$; for the scattering measurements $d>\sim 35$ and $k>7$. Therefore, we assume that the spherical reflection coefficient for both the reflection and the scattering measurements is comparable and very nearly equal to the plane wave coefficient. The measured reflection loss data ($-10\log(|R|)$) are shown in Fig. 17; and the values at the angles of interest are given in Table I.

TABLE I. Bottom loss (BL) estimates. the BL measured at site 2 includes the frequency band over which it was averaged (closest 1/3 band or bands) and the number of angles over which the data were averaged.

Frequency (Hz)	Angles (deg)	BL (dB) Derived from TS	BL (dB) Measured at Site 2
1800	39–47°	11.0±2.8	13.5±1.0; 1400–2200 Hz (11)
2400	44–48°	14.1±1.8	14.5±1.0; 2200–2800 Hz (5)
3600	47–51°	13.6±2.6	14.4±0.9; 3550–4470 Hz (3)

As a check on the assumption that using the measured reflection coefficient from Site 2 is reasonable near the MV, R_b can be computed in another way. Given the fact the angles between paths d and e are so similar, R_b can be estimated from the beam time series data at the MV as

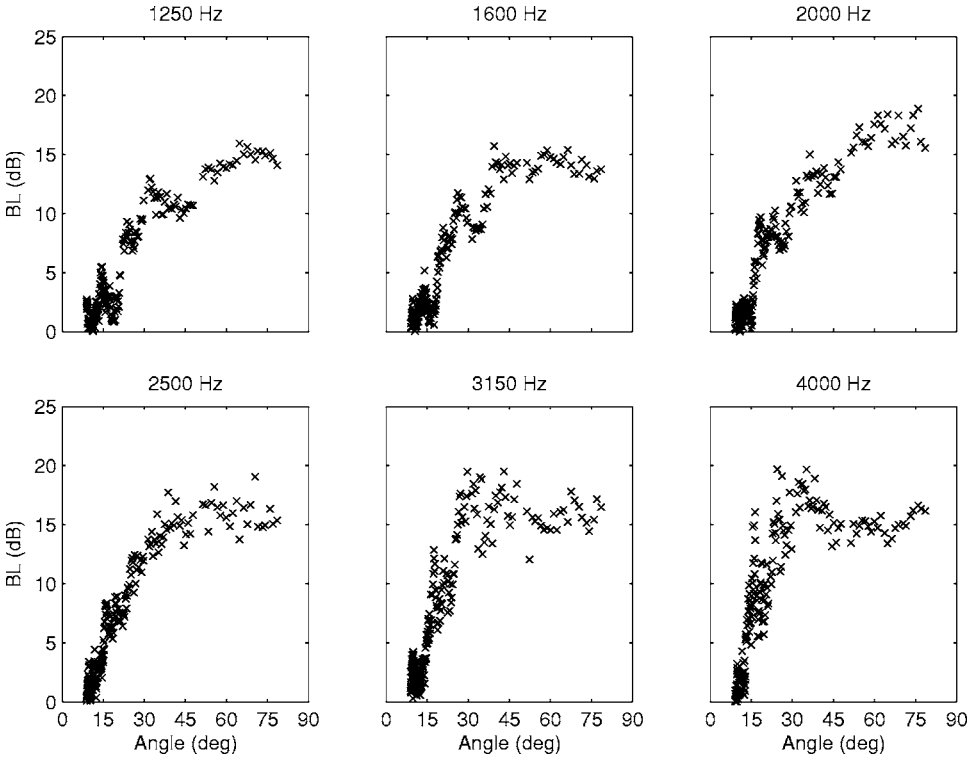

FIG. 17. Seabed reflection loss measured at Site 2 on the Malta Plateau. The data are averaged in 1/3 octave bins.

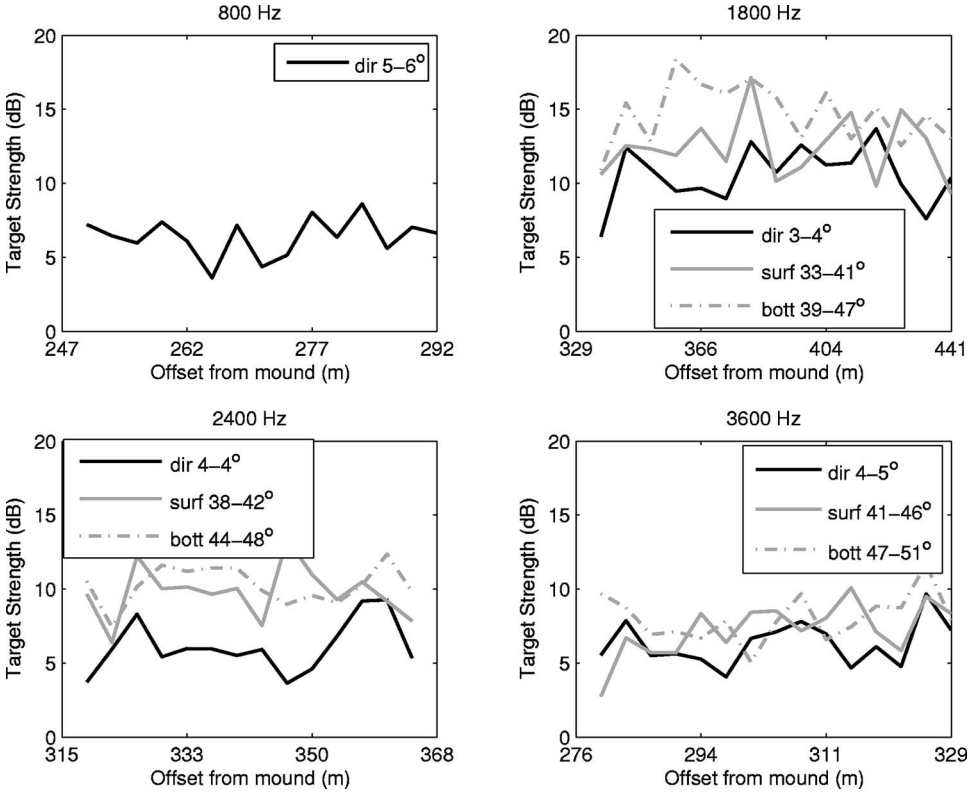

FIG. 18. Target strength of mound at Site 18 as a function of frequency, angle, and path. Monostatic (path a) is indicated by "*dir*," surface reflected path is indicated by "*surf*" and surface-bottom reflected is indicated by "*bott*."

$$R_b \simeq \frac{I_d}{I_e}\frac{\gamma_{\mathrm{se}}}{\gamma_{\mathrm{sd}}}, \tag{3}$$

where I_d and I_e are the received intensities from paths d and e, respectively, and γ_s is the transmission factor along the path from scatterer to receiver (although the transmission factors were computed, their ratio is very nearly unity since the paths are nearly identical at these ranges). The values of R_b derived in this fashion agree with those from Site 2 (see Table I) within the error bounds and thus give confidence that the reflection coefficient near the MV is similar that at Site 2.

For sea surface reflection we use (see Ref. 19)

$$|R_s(\theta,f)| = 1 - 0.21(k\sigma)^{3/2}\sin\theta, \tag{4}$$

where σ is the rms waveheight and the phase is assumed to be $-\pi$. The rms waveheight measured by a directional waverider buoy during the experimental period leads to $0.95 < |R_s(38-46^\circ, 1800-3600\ \mathrm{Hz})| < 1$.

The measured monostatic $(-)$ target strength computed with the model above is shown in Fig. 18. The grazing angles associated with the direct path (indicated by "*dir*") are provided in the legend. Also shown is the vertically bistatic target strengths (surface reflected path e) and (surface-bottom reflected path d) except at 800 Hz, where the beamwidths were too large for adequate spatial separation. In principle, we could have used the reciprocal paths b and c at 800 Hz, but in practice there was too much uncertainty in the path identification. The ordinate in Fig. 18 (offset from the MV) is estimated using the travel time. Note that each frequency has a distinct set of ranges/angles because the 15 pings for each frequency were transmitted serially (i.e., not interleaved). So Fig. 18 may depend upon geometry as well as frequency, although it should be noted that the angles at the various frequencies are quite similar.

There are several aspects of Fig. 18 that are important. First of all, note that the target strengths are fairly high, 4–14 dB, which means (in conjunction with its size) that the MV could be capable of producing clutter. Second, note that the scattering is fairly stable from ping to ping (one ping cycle is ~2.5 min) even though geometry is changing—grazing angles decreasing slightly with range. For each path type the standard deviation is typically less than 2 dB (see Table II). This stability suggests that the scattering mechanism is not hypersensitive to the precise geometry or geotime. This seems consistent with the evidence from the vertical array that the scattering mechanism is not due to bubble plumes in water column (which might lead to substantial temporal variability). This stability also indicates that there is a weak dependence of the scattering with vertical angle at least over a few degrees.

Third, note that in Fig. 18 (and Table II) that the target strength for paths a, e and d are similar. This suggests that the scattering may be nearly isotropic in the vertical, at least from 3° to 51° (although clearly the entire angular range is sparsely sampled). It is important to have some knowledge

TABLE II. Target strength (TS) estimates.

Frequency (Hz)	Monostatic TS (dB)	Surface-Direct TS (dB)	Surface-Direct-Bottom TS (dB)
800	6.1±1.6	⋯	⋯
1800	10.2±2.1	12.2±2.4	14.7±2.1
2400	6.0±1.7	9.9±1.7	10.3±1.3
3600	6.3±1.5	7.2±1.8	8.0±1.6

TABLE III. Properties of mud volcano used for modeling scattering from a visco-elastic sphere.

Set	Compressional speed (m/s)	Shear speed (m/s)	Compressional attenuation (dB/m/kHz)	Shear attenuation (dB/m/kHz)	Density (g/cm^3)
1	2200	1000	0.1	20	2.2
2	4000	1800	0.02	0.3	2.2

about the vertical angle dependence of the scattering for two reasons: (1) the dependence may help eliminate hypotheses about the scattering mechanism and (2) once the scattering mechanism is understood it may help suggest a reasonable physical model.

D. Simple modeling

The most likely scattering mechanism being the carbonate chimneys coupled with the nearly isotropic behavior of the scattering suggested that to first order, the MV might be considered as a visco-elastic sphere. The expressions developed by Faran[20] for an elastic sphere were extended to the visco-elastic case by allowing the wave number to become complex. The solution is written as an infinite sum of spherical basis functions; for the following cases 60 terms were sufficient to achieve convergence.

The fact that the carbonate chimneys cast a sharp shadow (see Fig. 4) is indicative of consolidated sediment, which we assume is carbonate. Since the carbonate properties are not known, we have used two plausible "end members" as listed in Table III. The theory is compared with the measured target strengths in Fig. 19 where it should be noted that the overall levels of the target strength are not very sensitive to the material properties. The theoretical target strength has the familiar shape with Rayleigh scattering rising as k^4 below $ka_o \sim 1$ (a_o is radius) and a roughly constant value above. The overall level is mostly controlled by the radius and scales approximately as a_o^2. The theoretical target strength for radius of $a_o=5$ m corresponding to the radii of the observed carbonate chimneys is in reasonable agreement with the measurements.

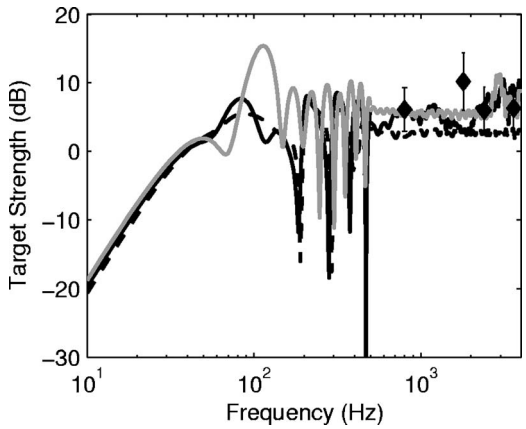

FIG. 19. Theoretical predictions of scattering from a visco-elastic sphere (solid and dashed lines) and measured monostatic data (♦) with ±2 standard deviations (I). The monostatic path is the solid black line and the vertically bistatic path (path *e* with 40° difference in incident and scattered angle) is the black dashed line. The gray line shows the monostatic path for geoparameter set 2 (see Table III). Above 500 Hz, the theoretical predictions are averaged over 200 Hz, commensurate with the data.

Both the monostatic target strength and the vertically bistatic target strength (relative angle difference of 40°) were computed and are shown in Fig. 19. Only the monostatic data are shown. While the data indicate that the vertically bistatic TS is a few dB lower than the monostatic case (Table II), the theoretical model for the sphere predicts the converse (Fig. 19)—though in a gross sense both the measurements and the model predict a weak dependence on vertical bistatic angle.

Though it may not be possible to draw absolute conclusions from the modeling, the results (i.e., agreement between model and data) are in accordance with and help substantiate the hypothesis that the scattering comes from the carbonate chimneys (Fig. 4). These features have dimensions close to that of the proxy sphere: lateral radial dimension of ~5 m and heights of around 2–4 m. Recall that the pulse in water has a radial dimension of 11 m, so one or several protrusions might be insonified at a given instant in time. The occurrence of multiple highlights in some pings (see Fig. 14) could arise from scattering from multiple protrusions spaced far enough apart to be temporally resolved. While the multiple highlights could also arise from near specular scattering from various facets or curved surfaces on the mound, facets and curved surfaces would not necessarily be expected to result in isotropic scattering in the vertical plane. In summary, the sphere model certainly adds weight to, but does not necessarily prove, the carbonate chimney scattering mechanism hypothesis. At the very least, the sphere model can be considered as a simple proxy, producing approximately the right levels as a function of frequency and angle.

V. SUMMARY AND CONCLUSIONS

Target strength measurements on an individual mud volcano indicate that it (and by extension other MVs) are a potential source of clutter for active sonar. Target strengths of 4–14 dB were observed from 800 to 3600 Hz for a monostatic geometry with grazing angles of 3–5°. Similar target strengths were measured for vertically bistatic paths with incident grazing angles of 3–5° and scattered angles of 33–50°. The target strengths were not very sensitive to precise geometry or geotime; typical standard deviations were ±2 dB over distances of tens of meters and order minutes.

The dominant scattering mechanism for this MV appears to be scattering from the protruding carbonate chimneys; free gas bubbles did not play a significant role. However, since ebullition of bubbles, particulates and fluids from MVs may be episodic, scattering from bubbles and particulates may be important for this particular MV at other times (perhaps associated with regional seismic events) and for other MVs in general. A simple visco-elastic model predicts reasonable first-order dependencies of the scattering as a function of frequency and vertical bistatic angle. With multibeam coverage over a larger area, we plan to develop a statistical clutter model based on the initial simple model developed here.

The short-range scattering measurement technique itself may be of importance to the community inasmuch as it is a fairly general way to probe small-scale features, dimensions of O(10–100) m. The key advantages of the technique (as compared to long-range techniques) are that: (a) the uncertainties associated with propagation through a generally sparsely sampled ocean are minimized, and (b) the proximity to the feature allows measurement geometries and concomitant analysis that can directly test hypotheses about the scattering mechanisms. One potential challenge with a vertical array (insonification is over 2π) is that the feature of interest must have a large scattering cross section compared to the background sediment. However, in practice, this is not expected to be a serious limitation since interest in clutter is focused on those features that have a high scattering cross section.

Future work will focus on the interpretation of long-range scattering from this same mud volcano. The observation that the scattering is nearly isotropic in the vertical plane should simplify that analysis inasmuch as the simple metric target strength can be employed.

ACKNOWLEDGMENTS

This research was supported by the Office of Naval Research in collaboration with the NATO Undersea Research Centre (NURC) under whose auspices the data were collected during experiment campaigns in 1998, 2002 and 2004. The authors express appreciation to Peter Nielsen, Chief Scientist of the Boundary 2002, Boundary 2004 Experiments under the aegis of the Boundary Characterization Joint Research Project, as well as the NURC ocean engineering personnel, the officers and crew of the *R/V Alliance* and the *ITS Tavolara* from which the GAS-SCIPACK measurements were performed.

[1]P. Ratilal, Y. Lai, D. Symonds, L. Ruhlman, J. Goff, C. Holland, J. R. Preston, E. Scheer, M. Sundvik, and N. Makris, "Long-range acoustic imaging of the continental shelf environment: the Acoustic Clutter Reconnaisance Experiment 2001," J. Acoust. Soc. Am. **117**, 1977–1998 (2005).

[2]M. K. Prior, "A scatterer map for the Malta Plateau," IEEE J. Ocean. Eng. **30**, 676–690 (2005).

[3]C. W. Holland, "Mapping seabed variability: Rapid surveying of coastal regions," J. Acoust. Soc. Am. **119**, 1373–1387 (2006).

[4]G. Etiope and A. V. Milkov, "A new estimate of global methane flux from onshore and shallow submarine mud volcanoes to the atmosphere," Envir. Geosciences **46**, 997–1002 (2004).

[5]A. V. Milkov, "Worldwide distribution of submarine mud volcanoes and associated gas hydrates," Mar. Geol. **167**, 29–42 (2000).

[6]G. Cifci, A. Limonov, L. Dimitrov, and V. Gainanov, "Mud volcanoes and dome-like structures an the Eastern Mediterranean Ridge," Mar. Geophys. Res. **19**, 421–438 (1997).

[7]C. W. Holland, G. Etiope, A. V. Milkov, E. Michelozzi, and P. Favali, "Mud volcanoes discovered offshore Sicily," Mar. Geol. **199**, 1–6 (2003).

[8]P. Yin, S. Berne, P. Vagner, B. Loubrieu, and Z. Liu, "Mud volcanoes at the shelf margin of the East China Sea," Mar. Geol. **194**, 135–149 (2003).

[9]G. Etiope, G. Marinaro, P. Favali, F. Furlan, S. Cenedese, and F. Gasparoni, "New technologies for methane leakage monitoring from seafloor-Description and first operational results," OMC-2005, Paper 177A, *Offshore Mediterranean Conference and Exhibition*, Ravenna, Italy, March 16–18, 2005.

[10]C. de Moustier and D. Alexandrou, "Angular dependence of 12 kHz seafloor acoustic backscatter," J. Acoust. Soc. Am. **90**, 522–531 (1991).

[11]G. Etiope, "Evaluation of a micro-gas chromatographic technique for environmental analyses of CO_2 and C_1–C_6 alkanes," J. Chromatogr. A 775, 243–249 (1997).

[12]G. Rehder, R. S. Keir, E. Suess, and T. Pohlmann, "The multiple sources and patterns of methane in North Sea waters," Aquat. Geochem. **4**, 403–427 (1998).

[13]M. Hovland and A. G. Judd, *Seabed Pockmarks and Seepage* (Graham and Trotman, London, 1988), p. 293.

[14]I. Leifer and R. Patro, "The bubble mechanism for methane transport from the shallow sea bed to the surface: A review and sensitivity study," Continental Shelf Res. **22**, 2409–2428 (2002).

[15]C. W. Holland, R. Hollett, and L. Troiano, "A measurement technique for bottom scattering in shallow water," J. Acoust. Soc. Am. **108**, 997–1011 (2000).

[16]P. Sylva, P. Menard, and D. Roy, "A reconfigurable real-time interpolation beamformer," IEEE J. Ocean. Eng. **11**, 123–126 (1986).

[17]C. W. Holland, "Shallow water coupled scattering and reflection measurements," IEEE J. Ocean. Eng. **27**, 454–470 (2002).

[18]For the monostatic case, two of the paths (direct-bottom and bottom-direct) arrive at the same instant in time, however, the incoherent assumption might still be reasonable since the incident and scattered angles are different for the two paths; thus the phases are not expected to be identical. If the two paths did sum completely coherently, the transmission loss would be 1.8 dB lower than modeled here.

[19]F. Li, J. Liu, and R. Zhang, "A model/data comparison for shallow-water reverberation," IEEE J. Ocean. Eng. **29**, 1060–1066 (2004).

[20]J. F. Faran, "Sound scattering by solid cylinders and spheres," J. Acoust. Soc. Am. **23**, 405–418 (1951).